Climate Dynamics

Century-scale variability in a randomly forced, two-dimensional thermohaline ocean circulation model

LA Mysak, TF Stocker*, and F Huang

Department of Atmospheric and Oceanic Sciences and Centre for Climate and Global Change Research, McGill University, 805 Sherbrooke St. W., Montreal, Quebec H3A 2K6, Canada

Abstract. The response of a two-dimensional thermohaline ocean circulation model to a random freshwater flux superimposed on the usual mixed boundary conditions for temperature and salinity is considered. It is shown that for a wide range of vertical and horizontal diffusivities and a box geometry that approximates the Atlantic Ocean, 200–300 yr period oscillations exist in the basic-state, interhemispheric meridional overturning circulation with deep convection in the north. These fluctuations can also be described in terms of propagating salinity anomalies which travel in the direction of the thermohaline flow. For large horizontal ($K_h = 15 \times 10^3$ m^2/s) and small vertical ($K_v = 0.5 \times 10^{-4}$ m^2/s) diffusivities, the random forcing also excites deca-millennial oscillations in the basic structure of the thermohaline circulation. In this case, the meridional circulation pattern slowly oscillates between three different stages: a large positive cell, with deep convection in the North Atlantic and upwelling in the south; a symmetric two-cell circulation, with deep convection in both polar regions and upwelling near the equator; and a large negative cell, with deep convection in the South Atlantic and upwelling in the north. Each state can persist for 0 (10 kyr).

Introduction

To summarize and increase our understanding of the nature and causes of century-scale climatic variability during the Holocene, Stocker and Mysak (1992, hereafter referred to as SM) recently presented a review of various high-resolution proxy data records. Since substantial humankind-induced global warming is expected to occur on this time scale, it is necessary to obtain further knowledge of natural century-scale climatic variability in order to be able to separate out the warming signal

from fluctuations that are inherent in the climate system. In the spectra of time series of proxy data derived from oxygen isotope ratios in ice cores, tree ring indices, pollen counts in lake sediments and sea-ice extents, SM found signifciant cyclic variations with time scales ranging from 50 to 400 yr. These signals were particularly evident in data gathered from locations around the North Atlantic (SM, Fig. 13), which suggests that this may be an important region of climatic variability on this time scale. On the basis of preliminary modelling results, SM speculated that such variability, rather than being externally forced by solar variations say, may be due to natural fluctuations in the basic-state thermohaline circulation of the ocean, which produce century-scale oscillations in the ocean-to-atmosphere heat flux.

The main purpose of this paper is to explore further this hypothesis by presenting modelling results using the one-basin (Atlantic Ocean) version of the thermohaline ocean circulation model of ==Wright and Stocker (1991,== herafter referred to as WS). This latitude-depth model, for the *zonally averaged* flow in an interhemispheric (pole-to-pole) basin (see Fig. 4 in WS), is based on the diagnostic equations of momentum and mass, and the time-dependent advection-diffusion equations of heat and salt. In order to excite the natural oscillations associated with the deep thermohaline circulation, the surface freshwater forcing varies randomly in time about the steady value.

We note here that zonally averaged models of the thermohaline circulation are generally not suitable for the study of decadal-scale ocean climate fluctuations because the latter centrally involve gyre-scale advective processes (Dickson et al. 1988; Mysak and Manak 1989; Mysak et al. 1990; Weaver and Sarachik 1991a, 1991b). Such processes are not resolved in the type of model considered in this paper. However, zonally averaged models can be profitably used (Stocker and Wright 1991a and 1991b, hereafter referred to as SW1 and SW2, respectively) to investigate the stability of the global "conveyor belt" circulation (e.g. Gordon 1986; Broecker et al. 1988) and the onset and evolution of oth-

* Current affiliation: Lamont-Doherty Geological Observatory of Columbia University, Palisades, NY 10964, USA

Correspondence to: LA Mysak

er century and longer time scale paleoclimatic phenomena which centrally involve global-scale convective overturning motions (Stocker et al. 1992).

This paper builds on several earlier modelling studies of the thermohaline circulation. These investigations generally fall into one of two categories: (1) those that describe the existence and the stability of various equilibria (or modes) for the circulation (e.g., Stommel 1961; Rooth 1982; Bryan 1986; Marotzke et al. 1988; Manabe and Stouffer 1988 (which involves a coupled ocean-atmosphere model); SW1; Weaver and Sarachik 1991a); (2) those that deal with natural oscillations about a stable mode of the thermohaline circulation (e.g. Mikolajewicz and Maier-Reimer 1990; Weaver and Sarachik 1991b; SM).

This paper falls mainly into the second category and particularily relates to the study of Mikolajewicz and Maier-Reimer (1990, hereafter referred to as MM-R), who describe the results of a numerical experiment in which a three-dimensional global ocean circulation model was driven by a spatially correlated white-noise freshwater flux superimposed on the climatological fluxes. MM-R found that in addition to the general red-noise character of the oceanic response, the model exhibits a pronounced low-frequency signal at around 320 yr, with centers of action in the Southern Ocean and the North Atlantic.

However, our study differs from MM-R in some important respects. Apart from the simpler geometry used here (only a two-dimensional version of the Atlantic Ocean without topography is employed), we also note two other distinctions: the freshwater random forcing used, while white-noise in form, is not spatially correlated; secondly, the model response is investigated for a wide range of horizontal and vertical diffusivities. The strength and structure of the steady thermohaline circulation depends strongly on the horizontal and the vertical diffusivities (Bryan 1987); hence it is natural to ask whether century-scale oscillations of MM-R type occur for a wide range of diffusivities, and also, whether fluctuations on other time scales can exist. These questions cannot easily be resolved with three-dimensional models because of computational limitations.

While the main goal of this research is to study century-scale fluctuations, in the course of the analysis it was found that for a relatively large value of the horizontal diffusivity ($K_h = 1.5 \times 10^4$ m^2/s), the model also contains large-amplitude, deca-millennial scale oscillations which can be characterized as "flips" between different modes of a relatively weak thermohaline circulation. Further, these very slow oscillations cause the cross-equatorial heat flux to change sign, which suggests that this type of variability may shed light on the O (10 kyr) paleoclimate fluctuations (1 kyr = 1000 yr) that have been investigated by Broecker and Denton (1989), Berger et al. (1991), Yiou et al. (1991) and others quoted therein. Indeed, to understand these long-term oscillations, it may be necessary to invoke the full range of *internal* variability of the climate system, which is in contrast to the concept of regarding it mainly as a "nonlinear climatic oscillator" forced by variations of the

Earth's orbital parameters (e.g., Pestiaux et al. 1988; Saltzman 1990).

The outline of this report is a follows. In the second section the ocean model is described. In the third section the numerical experiments are outlined, and the basic-state, interhemispheric meridional overturning circulation is described. A variety of solutions under random forcing superimposed on the steady boundary conditions are given in the fourth section. A discussion of salinity anomaly propagation associated with the approximately 200-yr oscillation which occurs in the model for a range of values of the diffusivities is presented in the fifth section. Finally, a summary and some concluding remarks are given in the last section.

The ocean model

The ocean circulation model employed here was developed by WS for use in paleoclimatic studies and builds on an earlier two-dimensional model of Marotzke et al. (1988). It is a zonally averaged, bouyancy driven model for the annual mean thermohaline circulation in an interhemispheric basin with a flat bottom. The model is based on the diagnostic equations of horizontal momentum, the hydrostatic approximation, the prognostic equations for heat and salt (with the same horizontal and vertical diffusivities in each equation) and a nonlinear, pressure-independent equation of state. The east-west pressure difference which arises upon averaging the momentum equations is taken to be proportional to the meridional pressure gradient, with a proportionality constant of 0.5. This parameterization is discussed and justified in WS. Although the seasonal cycle, wind stress and sea ice are not included in this model, SW1 show that the latitude-depth structure of temperature and salinity, as well as the meridional overturning rate compare reasonably well with observed estimates.

Satisfactory results for the large-scale flow can be obtained using a fairly coarse resolution, which makes the model suitable for long term integrations (thousands of years). We use a single basin of 60° width in longitude, which extends from 80° S to 80° N, and which is divided into 15 latitude bands. There are 9 vertical layers with the bottom of the layers being located at 70, 150, 250, 500, 1000, 2000, 3000, 4000 and 5000 m. The above spatial resolution permits a time step of about 14 days. Initially the ocean is at rest and has a uniform temperature of 4° C and a salinity of 35 ppt.

The model is first spun up from rest over a 2 kyr period by relaxing the temperature T and salinity S in the uppermost layer over a time scale of 70 days to:

$$T^* = 2 + 12.5 \ (1 + \cos \tfrac{1}{2} \pi s (1 + |s|)) \ (\text{in } °\text{C}), \qquad (1a)$$

$$S^* = 36 + \cos \pi s \ (\text{in ppt}), \qquad (1b)$$

where $s = \sin$ (latitude). Equation (1a) is an analytical approximation used by SW1 for the zonally averaged observed SST profile in the Atlantic (Levitus 1982), whereas (1b) is the simple sea surface salinity profile used by Marotzke et al. (1988) and WS. The resulting

(essentially) steady state consists of a symmetric two-cell circulation pattern with sinking in both polar regions (see WS Fig. 3a).

At year 2000 the vertical salt flux at the surface is diagnosed and then used as the boundary condition for S during a further 1 kyr integration period (the restoring boundary condition on T is retained). The symmetric two-cell circulation becomes unstable upon a switch to these mixed boundary conditions (Marotzke et al. 1988; WS), and a transition to a one-cell global circulation with deep water formation in only one high latitude region occurs. A small negative salinity anomaly (-0.1 ppt) is added to the surface of the southernmost grid box during this second integration period to obtain sinking in the northern hemisphere, which approximately characterizes the present-day thermohaline circulation in the Atlantic.

The experiments and basic steady states

A set of basic-state solutions under these steady mixed boundary conditions was first obtained for various horizontal and vertical diffusivities, which ranged from 1 to 15×10^3 m^2/s for K_h, and 0.5 to 5×10^{-4} m^2/s for K_v. Included in this range is a *canonical set of values*, namely, $K_h = 10^3$ m^2/s and $K_v = 10^{-4}$ m^2/s, which yields a circulation with a maximum meridional transport of about 18 Sv. This is comparable to the estimate of 17 Sv obtained from observations around $24°$N in the North Atlantic (Roemmich and Wunsch 1985).

For a given pair of diffusivities, a random freshwater flux was superimposed at 3 kyr on the basic-state freshwater flux (derived from the diagnosed salt flux) and the model was then run for another 5.5 kyr. The random forcing was white-noise in time and had the same amplitude in each grid box, namely, either 0.1 or 0.2 Sv; however, the area average of this forcing was zero at every time step. This precluded any net salt input into the system at any time. The value of 0.1 Sv is equivalent to a freshwater flux of about 500 mm/yr, which is comparable to the maximum diagnosed flux obtained for a mid-latitude grid box after the initial 2 kyr run. Smaller values of the random forcing were also employed (0.05, 0.025 and 0.01 Sv), and yielded smaller amplitude responses at similar frequencies. We opted for the larger values of the forcing amplitude in order to "shake the system vigorously", and bring out more clearly the full range of physical behaviour of the system under random forcing. In particular, the analysis of propagating salinity anomalies (fifth section) is facilitated using larger random forcing amplitudes. These cases also serve as limits to the possible evolution of the randomly forced system. More important, on short time scales (the time step in the model is 14 days), the selected amplitude of about 40 mm/month (corresponding to 0.1 Sv random forcing in each grid box) represents a reasonable amplitude.

MM-R used a weaker random white-noise forcing whose globally averaged standard deviation was about 190 mm/yr. In addition, to simulate the nature of large-
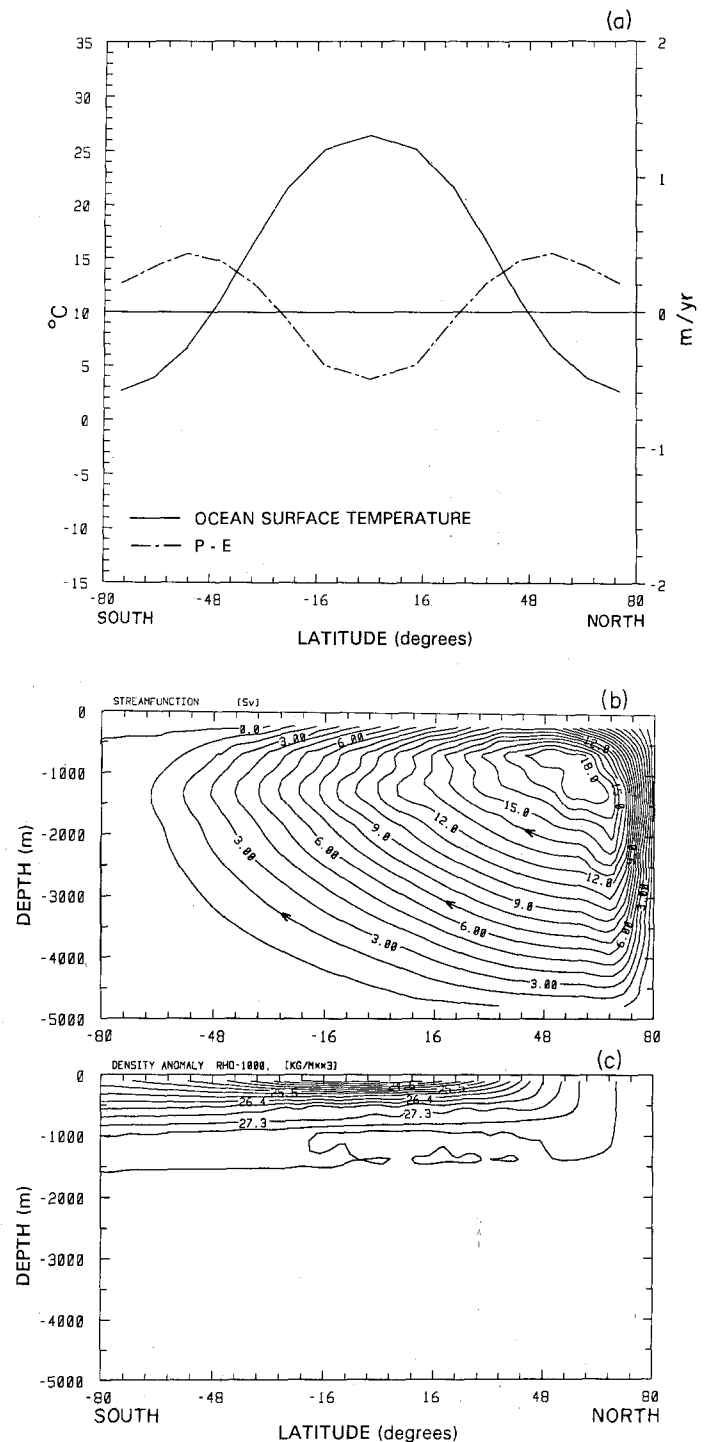

Fig. 1. a The steady mixed boundary conditions (restoring for temperature as per (**1a**) and freshwater flux for salinity as diagnosed after a 2 kyr (1 kyr = 1000 yr) initial integration period) for the canonical diffusivity pair ($K_h = 10^3$ m^2/s and $K_v = 10^{-4}$ m^2/s); **b** Contours of the meridional overturning streamfunction in Sverdrups (1 Sv = 10^6 m^3/s) at 3 kyr resulting from the application of boundary conditions in **a** for the period 2–3 kyr; **c** The density anomaly (i.e. $\rho - 1000$) in kg/m^3 at 3 kyr corresponding to the flow in **b**

scale two-dimensional weather patterns, their random forcing also had a horizontal correlation scale of about 3000 km.

Various quantities, such as the maximum and minimum values of the streamfunction, the depth-integrated meridional heat flux just north of the equator (at $7.5°$ N) and at $50°$ N, and the convection depth in each box, were stored every 5 years during the 5.5 kyr random forcing period. These time series were then used for statistical analysis. To check for aliasing due to this discrete sampling, we compared the results against those obtained from time series that were sampled every time step. No evidence of aliasing was found.

Figurer 1a shows the meridional profiles of the mixed boundary conditions that were applied to generate the basic-state thermohaline flow seen in Fig. 1b for the case $K_h = 10^3$ m^2/s and $K_v = 10^{-4}$ m^2/s, the canonical values for the diffusivities. This flow has a maximum transport of 18.3 Sv and a maximum (depth-averaged) meridional heat flux of 0.915 PW in the low latitudes, which are consistent with observations in the North Atlantic. Figure 1c shows the corresponding density field at 3 kyr and clearly reveals a well-mixed region from the surface down to the bottom in the high northern latitudes, where there is deep convection. In the southern latitudes, the flow is characterized mainly by a slow upward motion.

Results of the type shown in Fig. 1b, c were obtained for many pairs of diffusivities, and the properities of these are summarized in Tables 1 and 2, which give the maximum transport and maximum meridional heat flux in each case. Consistent with other studies (e.g. Bryan 1987; Wright and Stocker 1992), we observe that the transport increases with K_v (for fixed K_h): over the range of a ten-fold increase in the vertical diffusivity, the maximum transport monotonically increases approximately four-fold. From Table 1 we note, however, that for fixed K_v, the transport decreases fairly slowly with *increasing* K_h: for a fifteen-fold increase in this parameter the transport drops by about 30 to 40%. This behaviour is due to the fact that a larger K_h tends to reduce the meridional density gradient, which is the basic driving mechanism for the thermohaline circulation.

From Table 2 we observe that the meridional heat flux changes with the diffusivities in the same general way as in the case of the transport, but more gradually. However, as K_h approaches very large values for small fixed K_v, the maximum heat flux starts to increase rather than continuing to decrease. This is because for large K_h, in conjunction with the coarse resolution and weak overturning, the diffusive part of the meridional heat flux begins to dominate the advective part.

Randomly forced solutions

Basic statistics

From Table 3, which shows $\langle \psi \rangle$, the time mean of the maximum streamfunction time series for various pairs of diffusivities, we note that the basic flow (one large positive meridional overturning cell as seen in Fig. 1b) is generally stable to the random forcing (of 0.1 Sv in each grid box) with mean values that are generally slightly

Table 1. Maximum values of the streamfunction (in Sv) at 3 kyr for various pairs of diffusivities. The overturning transport decreases for increasing K_h because the latter change reduces the meridional density gradient

K_v (10^{-4} m^2/s) ↓	K_h (10^3 m^2/s) →				
	1	2	5	10	15
0.5	11.8	11.2	10.2	7.89	7.58
1.0	18.3	17.8	16.4	13.5	11.2
2.0	27.9	27.3	25.7	23.2	16.5
5.0	47.4	46.5	44.4	40.6	30.7

Table 2. Maximum depth-integrated meridional heat flux (in PW) at 3 kyr for various pairs of diffusivities

K_v (10^{-4} m^2/s) ↓	K_h (10^3 m^2/s) →				
	1	2	5	10	15
0.5	0.625	0.610	0.594	0.553	0.651
1.0	0.915	0.894	0.861	0.802	0.816
2.0	1.31	1.29	1.23	1.23	1.05
5.0	2.07	2.02	1.93	1.87	1.61

Table 3. Mean ($\langle \psi \rangle$) and standard deviation (σ) of time series of maximum streamfunction for the randomly forced period 3–8.5 kyr for various pairs of diffusivities. The random (white-noise) freshwater flux has an amplitude of 0.1 Sv im each grid box. For each fixed K_v, the two lines of numbers represent respectively $\langle \psi \rangle$ (in Sv) and σ (in Sv)

K_v (10^{-4} m^2/s) ↓	K_h (10^3 m^2/s) →				
	1	2	5	10	15
0.5	12.65[a]	12.04	10.67	8.98	5.49
	1.84[b]	1.37	0.76	0.44	0.77
1.0	18.50	17.97	16.64	14.81	11.93
	0.71	0.74	0.68	0.69	0.37
2.0	27.90	27.35	25.76	23.32	20.13
	0.33	0.32	0.21	0.18	0.29
5.0	47.62	46.92	44.40	40.57	22.13
	0.20	0.20	0.20	0.19	0.18

[a] $\langle \psi \rangle$
[b] σ

larger than those in Table 1. However, for $K_h = 15 \times 10^3$ m^2/s and both $K_v = 0.5$ and 5×10^{-4} m^2/s, $\langle \psi \rangle$ has actually decreased substantially because under random forcing the one-cell circulation pattern reverts back to a symmetric two-cell pattern with a maximum transport in each hemisphere that is weaker than that in a one-cell pattern.

The amplitude of the fluctuations under random forcing is characterized by the standard deviation σ; the values of σ for the maximum streamfunction time series are listed in Table 3 under the mean values. Note that σ

Table 4. Mean $[\langle F_1\rangle]$ and standard deviation (σ_1) of time series of depth-integrated meridional heat flux across $7.5°$N (F_1), for the randomly forced period 3–8.5 kyr for various pairs of diffusivities. The random (white-noise) freshwater flux has an amplitude of 0.1 Sv in each grid box. For each fixed K_v, the two lines of numbers present respectively $\langle F_1\rangle$ (in PW) and σ_1 $(10^{-2}$ PW)

K_v $(10^{-4}$ m^2/s) ↓	K_h $(10^3$ m^2/s) →				
	1	2	5	10	15
0.5	0.48[a]	0.46	0.41	0.37	0.19
	2.88[b]	2.45	1.52	0.93	4.25
1.09	0.71	0.68	0.61	0.55	0.44
	1.18	1.34	1.24	1.32	2.05
2.0	1.02	0.98	0.88	0.80	0.70
	0.53	0.52	0.47	0.39	2.19
5.0	1.58	1.53	1.39	1.23	0.42
	0.47	0.47	0.44	0.39	0.52

[a] $\langle F_1\rangle$
[b] σ_1

is generally less than 10% of $\langle\psi\rangle$ and that σ drops substantially as K_v increases, i.e. the oscillations are strongly damped for large diffusivities.

The mean and standard deviation of the randomly forced meridional heat flux at $7.5°$N (F_1) for various diffusivities are given in Table 4. For fixed K_v, F_1 varies slowly with K_h up to 10×10^3 m^2/s. For large and small K_v and large K_h, however, F_1 drops substantially due to small cross-equatorial flow in the two-cell circulation which has formed in response to the introduction of the random forcing. From Table 4 we also note that except for the case of small K_v and large K_h, the standard deviations are quite small (typically a few percent of F_1).

Similar experiments were performed with random forcing amplitudes in the range of 0.01 to 0.2 Sv. Generally, the mean values of the maximum streamfunction did not differ by more than 2% from the values given in Table 3. The standard deviations, as expected, increased in an approximately linear fashion with increasing forcing amplitude.

Fig. 2a–d. 5.5 kyr time series of **a** maximum (*solid*) and minimum (*dashed*) streamfunction; **b** depth-integrated meridional heat flux F_1 (at $7.5°$N); **c** depth-integrated meridional heat flux F_2 (at $50°$N); and **d** convection depth in the northernmost grid box column (70–80°N) for the case of the canonical diffusivity pair and a random forcing of 0.1 Sv in each grid box. The arrows E and E' mark the beginning (at year 6830) and end of the large 240-yr oscillation event that is described further in Fig. 3. The *arrows A* and A' bracket an approximately 208-yr oscillation beginning at year 5043 that is further described in Fig. 10

Time series

We first describe a selection of time series for the case of the canonical diffusivity values (Fig. 2). From Fig. 2a (solid line) we note that the maximum streamfunction time series (associated with the large positive cell), is dominated by a fairly regular sequence of oscillations with a period in the range of 200–250 yr. The amplitude of these ocsillations is approximately 5% of the mean, which is consistent with the standard deviation of 0.71 Sv given in Table 3. Oscillations of a similar time scale are also seen in the minimum (negative) streamfunction time series (Fig. 2a, dashed line), which describe the fluctuations in a small surface-intensified negative cell in the southern latitudes.
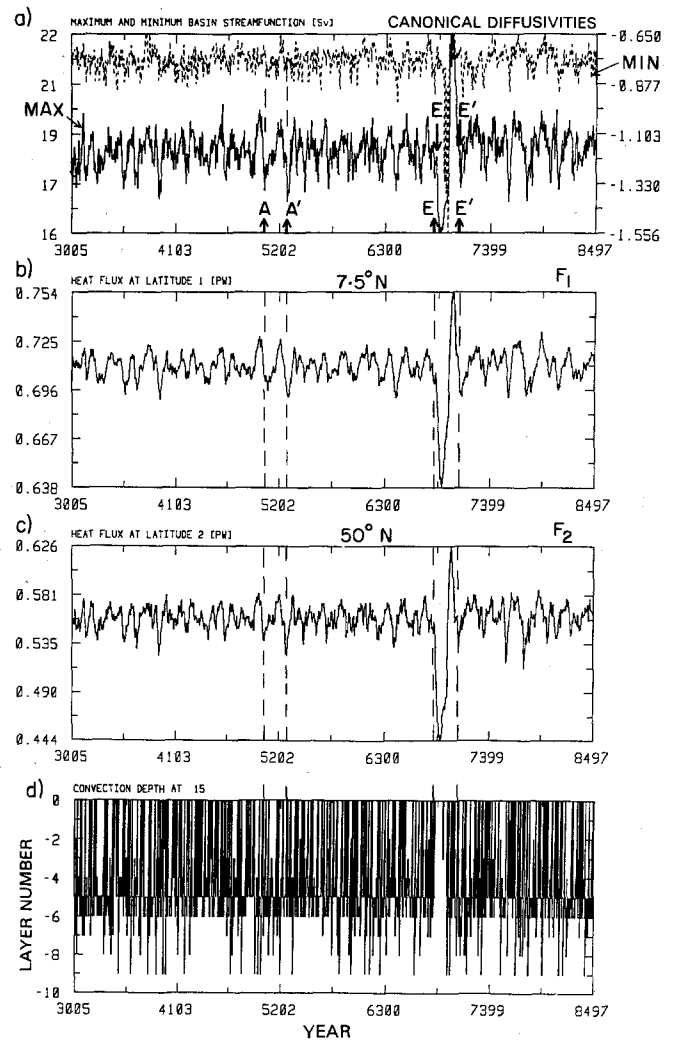
The maximum streamfunction time series also shows evidence of small-amplitude high-frequency motions (about 50 yr time scales), which can be seen in the time series for the minimum streamfunction as well. However, the high-frequency signals are less prevalent in the time series for the two meridional heat fluxes (Fig. 2b, c) because, in contrast to the case for the streamfunction maximum, the heat fluxes are sampled further south, away from the high-latitude regions where changes in convection depth have an immediate effect on the streamfunction.

The two heat flux time series are highly correlated, and as expected, each is positively correlated with the series for the maximum streamfunction; this is generally the case for time series for other diffusivities as well.

MERIDIONAL OVERTURNING

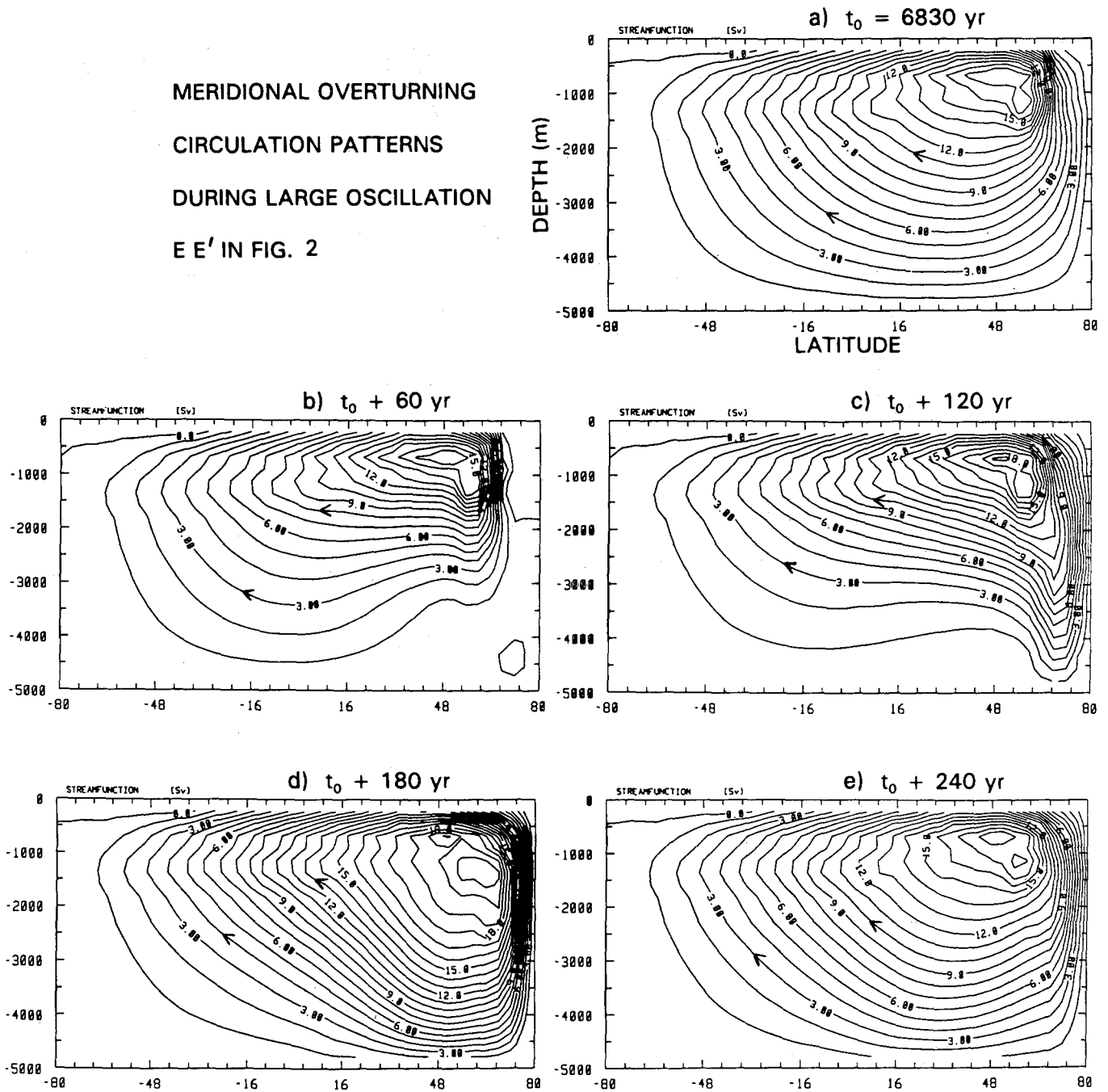CIRCULATION PATTERNS

DURING LARGE OSCILLATION

E E' IN FIG. 2

Fig. 3a–e. Streamfunction contours at 60-yr intervals which span the 240-yr oscillation EE' in Fig. 2. **a** $t = 6830$ yr $\equiv t_0$; **b** $t_0 + 60$ yr; **c** $t_0 + 120$ yr; **d** $t_0 + 180$ yr, and **e** $t_0 + 240$ yr (end of oscillation)

Henceforth, we shall focus mainly on the near-equatorial heat flux F_1 when describing the temporal behaviour of the solutions for other diffusivities.

Associated with the oscillations in the upper three panels of Fig. 2 are large fluctuations in the convection depth in the northernmost grid box column (Fig. 2d). While convection tends to occur most commonly between layers 4 and 6 (500 to 2000 m), as indicated by the many short heavy black vertical lines in this range, deep convection or no convection also happen occasionally.

One noticeable event in Fig. 2 is the large-amplitude 240-yr oscillation indicated by EE'. (The oscillation marked AA' will be described in the fifth section.) Around year 6830 the convection depth starts to decrease rapidly and then convection ceases for several decades (Fig. 2d). Consequently, the lighter water arriving from lower latitudes no longer sinks to the abyss, and hence there is a sudden large drop (about 15% of the mean) in the transport (Fig. 2a) with associated reductions in the meridional heat fluxes (Fig. 2b, c). After year 6950 (half a cycle later), deep convection starts again (Fig. 2d) and the transport becomes very strong. As a result, the maximum streamfunction time series overshoots the mean (see Fig. 2a), as do the time series

for the heat fluxes. However, by the year 7070 (end of cycle) all the time series have returned to around their mean values.

Figure 3 shows the evolution of the flow field over the course of the large-amplitude oscillation EE'. At time $t_0 = 6830$ yr (Fig. 3a), the flow pattern is "normal" (cf. Fig. 1b); but a quarter of a cycle later (Fig. 3b), the high-latitude convection zone has shifted south by one grid box and convection is now shallower because this zone has a more stably stratified water column than the northernmost one. During this phase the supply of low-latitude saline water is reduced and surface cooling provides a mechanism to enable deep convection to resume in the northernmost box. Hence on the rebound (half a cycle after time E), convection returns to this grid box and again extends down to the bottom (Fig. 3c). Sixty years later (Fig. 3d) convection is still deep and there is now substantial southward flow along the bottom. In Fig. 3e, at the end of the oscillation, the flow has returned to normal, being similar to that in Fig. 3a. Throughout the course of this event the ocean-to-atmosphere heat flux is near zero (although slightly positive) in the southern latitudes, and around -25 W/m^2 near the equator. However, in the northernmost grid box, the flux is 10–20 W/m^2 at the beginning of the oscillation and then rises to 60–75 W/m^2 during the middle of the cycle, indicating resumption of deep convection in this grid box. Such an increase in this heat flux would produce a high-latitude warming in the lower troposphere of about 3°C.

A higher vertical resolution run (with 15 layers) was also carried out for the canonical diffusivity pair and the same random forcing. Increasing the number of layers results in less numerical diffusion and thus reduces the effective vertical diffusivity and meridional overturning. Consequently, the mean of the time series for the maximum streamfunction was found to be slightly reduced (by about 5%), but the amplitude of the 200-yr fluctuations was still about 5% of the mean. The amplitude of the oscillation EE' was reduced, however, and the large drops in the heat fluxes were about 10% of the mean (instead of about 20% – see Fig. 2b, c).

To check the frequency of occurrence of the large oscillation EE' in Fig. 2, the model was run for a total of 100 kyr with the canonical diffusivity values and a random forcing amplitude of 0.1 Sv. Figure 4 shows the randomly forced time series for F_1, over the period 3–100 kyr, which is characteristic of the time series for other quantities. We note that the system is stable over this long time interval: the flow retains its large positive cell structure, but the large-amplitude oscillations are a recurrent phenomenon. However, the interval between these oscillations varies from about 2 to 8 kyr, and on the average about 4 large oscillations occur in every 20 kyr time span.

We now describe the temporal behaviour of the solutions for large K_h ($= 15 \times 10^3$ m^2/s) and either large K_v ($= 5 \times 10^{-4}$ m^2/s) or small K_v ($= 0.5 \times 10^{-4}$ m^2/s) when a random forcing of 0.1 Sv is applied. The mean values of the maximum streamfunction (see Table 3) and heat flux F_1 (see Table 4) were much lower than the respec-
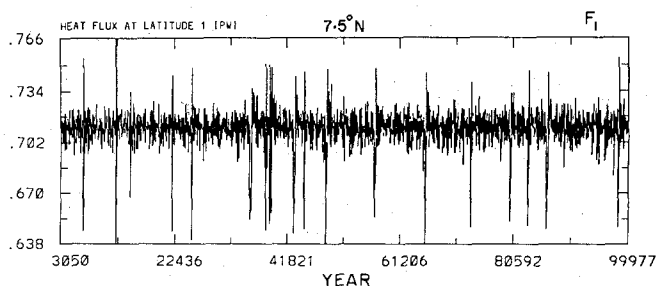

Fig. 4. As in Fig. 2b, except the random forcing period extends from 3 to 100 kyr

tive means for a slightly smaller K_h ($= 10^4$ m^2/s) because these solutions had switched from a large positive cell circulation to a symmetric two-cell circulation, with deep convection in both polar regions. For the case of large K_v, the transition occurred quickly (within 500 yr) after the random forcing was applied, and the standard deviations of the resulting oscillations were small (Tables 3 and 4), indicating a stable solution. For the case of small K_v, however, the transition to a two-cell circulation did not occur until around year 6000 and the standard deviations of the time series were relatively large (Tables 3 and 4). For both sets of diffusivity pairs, the same behaviour was also found for a 0.2 Sv random forcing.

To see whether the two-cell circulation pattern for small K_v (and large K_h) remained stable over a much longer time span, a 100-kyr run (with a random forcing of 0.1 Sv during the last 95 kyr) was carried out. The resulting 95-kyr time series (from data sampled every 50 yr) are shown in Fig. 5. (Similar time series were also found for a 0.2 Sv random forcing.)

Figure 5 indicates very clearly that over tens of thousands of years, the randomly forced solution for large K_h and small K_v undergoes large-amplitude oscillations between *three* quasi-stable states (or modes), which might be interpreted as attractors of the system: (1) the usual large positive cell circulation (e.g. at time A); (2) a symmetric two-cell circulation (e.g. at time B); and (3) a large *negative* cell circulation (e.g. at time C). Associated with each of these states are noticeably different cross-equatorial heat fluxes, ranging from around 0.3 PW at time A to near 0.0 PW at time C (Fig. 5b). These states last for 5–10 kyr, and since the transition between states is quite rapid (a few thousand years or less), the time series in Fig. 5 appears to be dominated by very large-amplitude 10–20 kyr oscillations. Superimposed on these large-amplitude oscillations are higher frequency signals with periods of a few hundred to a few thousand years. However, as we shall see in next section, the latter oscillations are not statistically significant. A 100-kyr run was also carried out for a slightly reduced K_h ($= 10^4$ m^2/s) and the same small K_v; in this case, the large-amplitude O (10-kyr) oscillations were not present in the time series.

The existence of each quasi-stable mode for only about 5–10 kyr is related to the fact that this is the time scale t_d associated with the vertical diffusivity coefficient
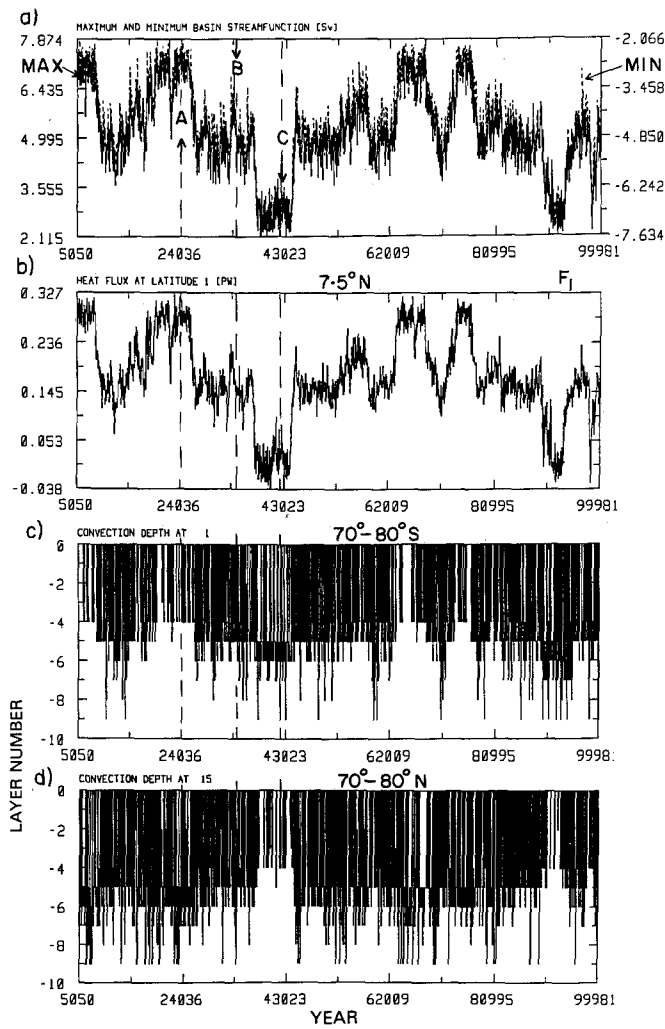
Fig. 5a–d. 95 kyr time series of **a** maximum (*solid*) and minimum (*dashed*) streamfunction; **b** heat flux F_1; **c** convection depth in the southernmost grid box column, and **d** convection depth in the northernmost grid box column for the case of the diffusivity pair $K_h = 15 \times 10^3 \ \text{m}^2/\text{s}$ and $K_v = 0.5 \times 10^{-4} \ \text{m}^2/\text{s}$ and a random forcing of 0.1 Sv in each grid box. The *arrows A, B* and *C* mark the times 24, 36 and 42 kyr respectively, at which instants the streamfunction contours are shown in Fig. 6. In this experiment the steady mixed boundary conditions were applied for the period 2–5 kyr, and the random forcing was added thereafter

Fig. 6a–c. Streamfunction contours at time instants *A, B* and *C* shown in Fig. 5. **a** 24 kyr; **b** 36 kyr and **c** 42 kyr

$(t_d = O(H^2/K_v))$, where $H = 10^3 \text{m}$, the ocean depth), and that diffusive processes on this time scale dominate the relatively weak advective processes that occur for large K_h (see Table 3). Thus, due to the slow downward diffusion of heat in a quiescent region, an instability develops after several thousand years, causing the circulation to flip into another mode. In addition, the random forcing renders the two-cell circulation for this diffusivity pair to be quasi-stable. Associated with the large swings between positive and negative cell circulation patterns is a complementary behaviour in the convection in the boundary grid box columns (see times A and C in Fig. 5c, d).

Instantaneous plots of the streamfunction contours at times A, B and C are shown in Fig. 6. In Fig. 6a we note that in addition to the large positive cell, there is
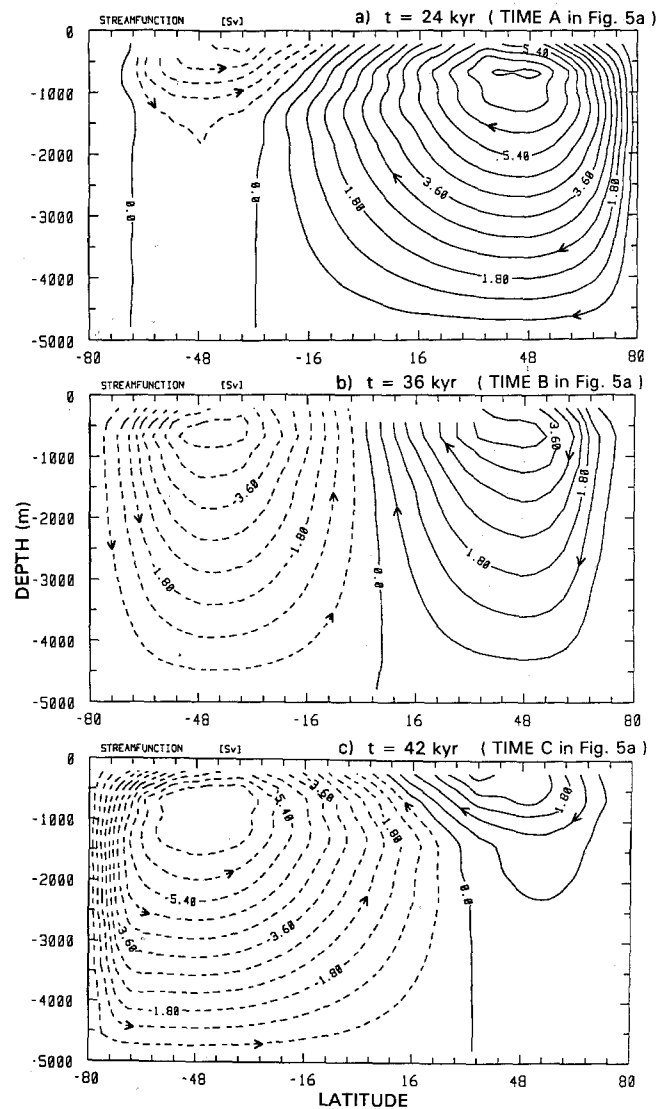
also a shallow negative cell centred around 48° S. However, convection is not very deep to the south of this latitude, and indeed, the density anomaly contours are horizontal at depths of around 1000–1500 m in these southern latitudes (similar to what is seen in Fig. 1c). Figure 6b depicts the symmetric two-cell state, and Fig. 6c, the large negative cell state with deep convection in the far south. Note also the shallow positive cell in the north for state 3; thus, this latter state is like the mirror image of state 1. For the symmetric two-cell circulation (state 2) the ocean-to-atmosphere heat flux is about the same in both polar regions.

Spectra

Each time series extending over 5500 years (1100 data points) was decomposed into a finite-sum Fourier series (1024 terms). From each series the spectrum was computed as the modulus of the coefficient vector from the
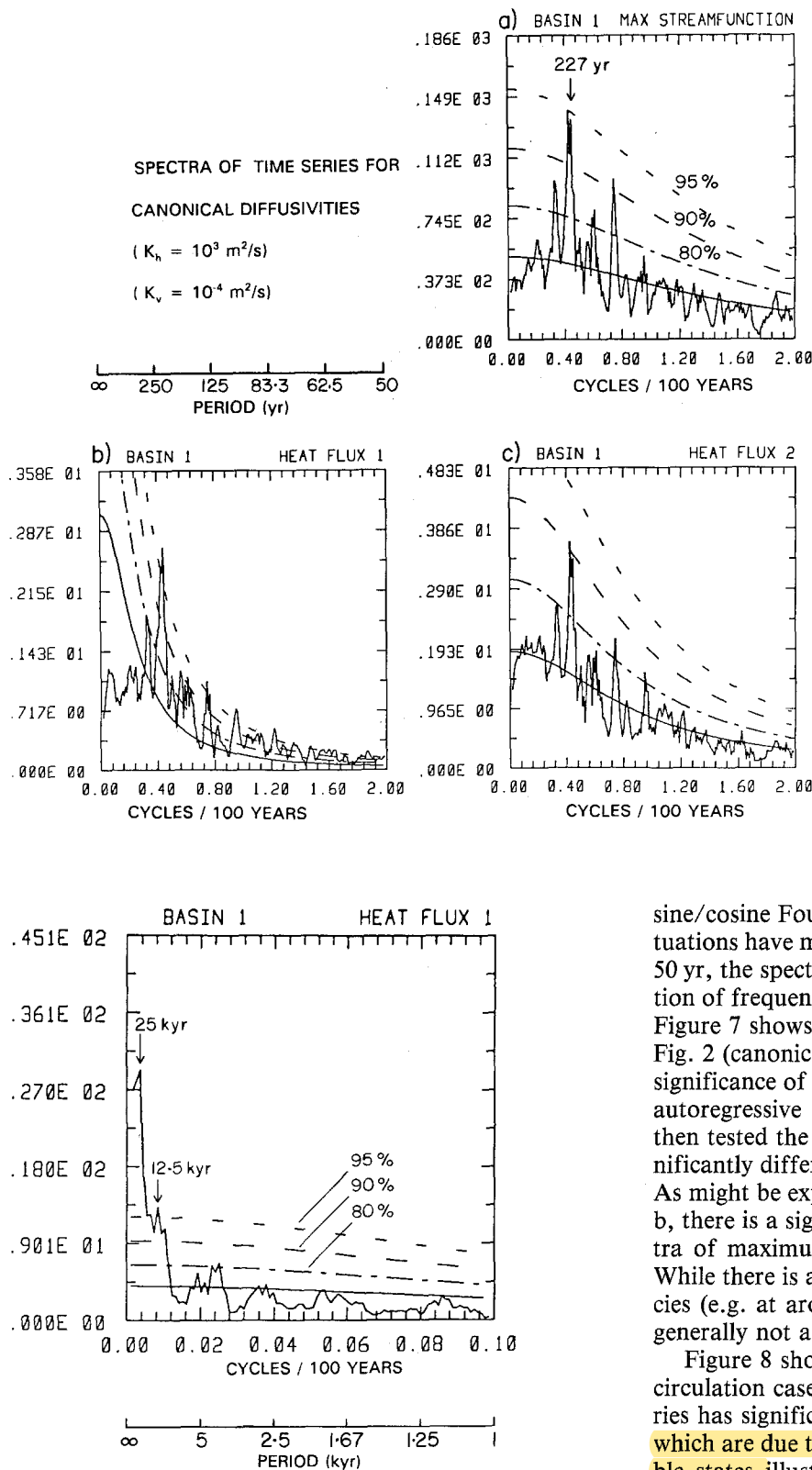
a) BASIN 1   MAX STREAMFUNCTION

SPECTRA OF TIME SERIES FOR

CANONICAL DIFFUSIVITIES

($K_h = 10^3$ m^2/s)

($K_v = 10^{-4}$ m^2/s)

227 yr

95%
90%
80%

.186E 03
.149E 03
.112E 03
.745E 02
.373E 02
.000E 00
0.00 0.40 0.80 1.20 1.60 2.00
CYCLES / 100 YEARS

∞   250   125   83·3   62·5   50
PERIOD (yr)

b) BASIN 1   HEAT FLUX 1

.358E 01
.287E 01
.215E 01
.143E 01
.717E 00
.000E 00
0.00 0.40 0.80 1.20 1.60 2.00
CYCLES / 100 YEARS

c) BASIN 1   HEAT FLUX 2

.483E 01
.386E 01
.290E 01
.193E 01
.965E 00
.000E 00
0.00 0.40 0.80 1.20 1.60 2.00
CYCLES / 100 YEARS

Fig. 7a–c. The three-point smoothed spectrum (square root of the sum of the squares of the Fourier coefficients) for each of the 5.5 kyr time series shown in Fig. 2a, b and c for the canonical diffusivity pair. The *dashed lines* indicate the 95, 90 and 80% confidence levels based on a first-order autoregressive process (*solid line*). The spectrum for the minimum streamfunction (not shown) does not have any significant peaks at the 90 or 95% level. Each spectrum has the units of the quantity specified at the *top* of the figure

BASIN 1   HEAT FLUX 1

.451E 02
.361E 02
.270E 02
.180E 02
.901E 01
.000E 00
0.00   0.02   0.04   0.06   0.08   0.10
CYCLES / 100 YEARS

25 kyr

12·5 kyr

95%
90%
80%

∞   5   2·5   1·67   1·25   1
PERIOD (kyr)

Fig. 8. Three-point smoothed spectrum of the 95-kyr time series shown in Fig. 5b (F_1 for the diffusivities $K_h = 15 \times 10^3$ m^2/s and $K_v = 0.5 \times 10^{-4}$ m^2/s)

sine/cosine Fourier series (Priestly 1989). Since the fluctuations have most of their energy at periods longer than 50 yr, the spectra (in most cases) were plotted as a function of frequency which ranged from 0 to 0.02 cycles/yr. Figure 7 shows the spectra of three of the time series in Fig. 2 (canonical diffusivity case). In order to assess the significance of various peaks in the spectra, a first-order autoregressive model was fitted to each spectrum. We then tested the hypothesis whether the time series is significantly different from red-noise (Mitchell et al. 1966). As might be expected from the time series in Fig. 2a and b, there is a significant peak at about 227 yr in the spectra of maximum streamfunction and the heat flux F_1. While there is also evidence of energy at higher frequencies (e.g. at around 140 yr), the peaks in this range are generally not as significant.

Figure 8 shows that for large K_h and small K_v (weak circulation case), the F_1 spectrum of the 95-kyr time series has significant peaks at periods of 25 and 12.5 kyr, which are due to the oscillations between the three possible states illustrated in Fig. 6. During the last glacial maximum, it is now believed (Boyle and Keigwin 1987) that deep water formation was reduced in the North Atlantic and hence that the thermohaline circulation was much weaker than today. If so, then it is tempting to speculate that these diffusivity values might have applied to the ocean during that time, and also possibly during the transition to the present warm (interglacial) period. In particular, it is interesting to note in Fig. 5b
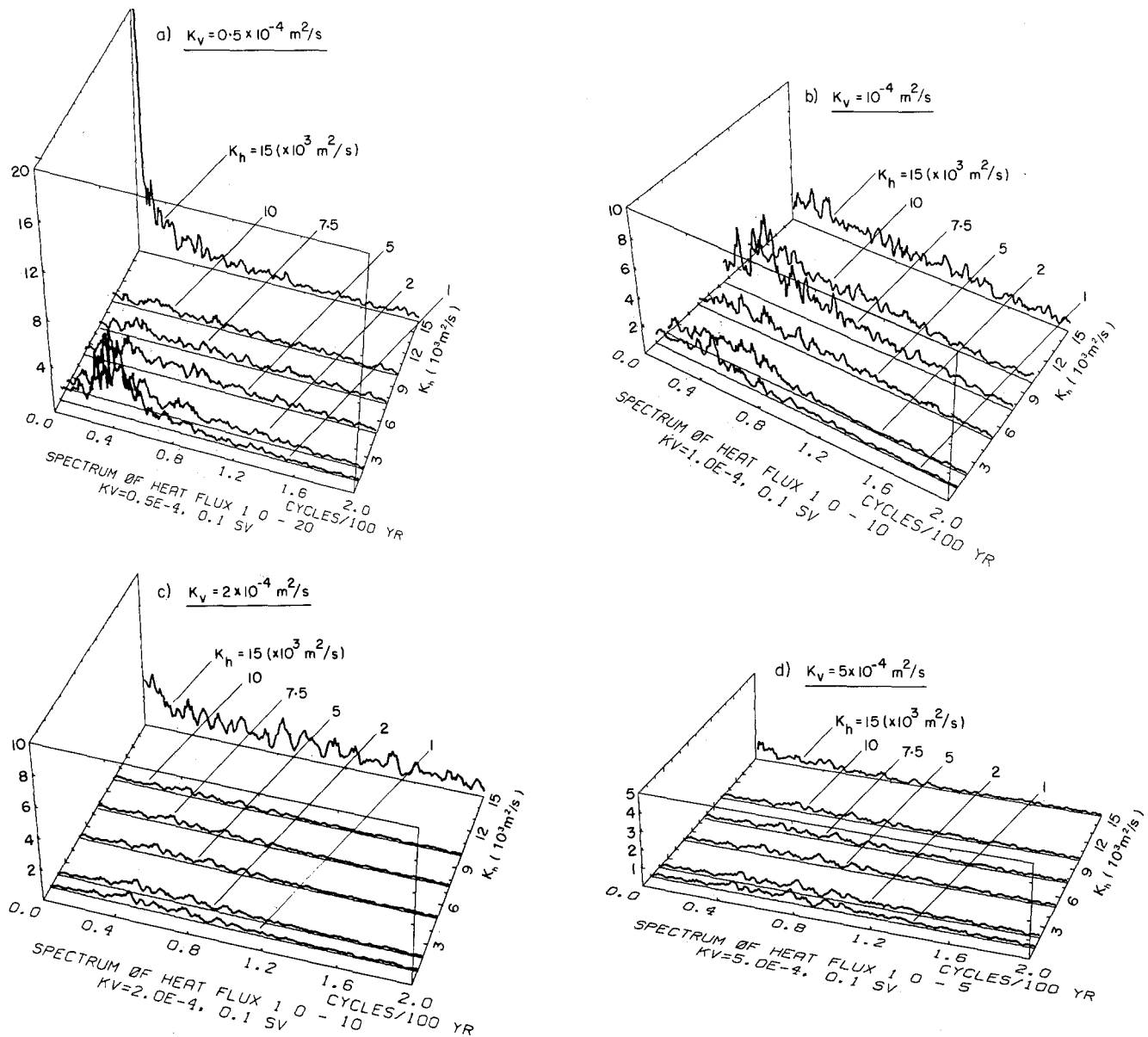
Fig. 9a–d. Spectra of the near-equatorial heat flux time series F_1 for 0.1 Sv random forcing over a 5.5 kyr period for fixed K_v and various values of K_h. **a** $K_v = 0.5 \times 10^{-4}\,\mathrm{m^2/s}$; **b** $K_v = 10^{-4}\,\mathrm{m^2/s}$; **c** $K_v = 2 \times 10^{-4}\,\mathrm{m^2/s}$; **d** $K_v = 5 \times 10^{-4}\,\mathrm{m^2/s}$

the rapid Northern Hemisphere warming just after year 43 000 as implied by the increase in F_1 and the concurrent transition to the two-cell circulation state (see Fig. 5a). Then around year 52 000 there is another warming, followed by a sudden cooling, and finally, a fairly large warming after year 62 000, which is accompanied by a transition to a positive one-cell circulation. Although this pattern of warming, cooling and warming is stretched out over 18 kyr, it is similar to that which occurred during the last glacial-interglacial transition (which included short warming and cooling periods). In reality, however, the sequence of observed changes took place in less than 10 kyr (Broecker and Denton 1989), about half the time period described. Nonetheless the results suggest that, although the random forcing has no intrinsic time scale, it is able to excite very long-period oscillations in the climate system through the interaction of diffusive and advective processes in different parts of

the deep ocean. A characteristic of such a behaviour is the fact that the transitions between states are rapid and that individual states can appear stable for several thousands of years. Although we do not attempt to apply these findings directly to the observed record (because the present model is too idealized; for example, there is only one ocean basin and no land ice, which could play an important role), the behaviour is instructive and corroborates earlier work that suggests that atmospheric freshwater fluxes could be important for major climate changes (Broecker and Denton 1989; WS2).

To gain an overview of the sensitivity of the frequency response of the randomly forced model to a change in the diffusivity values, we have plotted in each part of Fig. 9, a K_h-family of spectra of F_1 corresponding to a fixed value of K_v. Thus in Fig. 9a for example, the six spectra shown correspond to the case of small K_v and K_h ranging over six values. In this figure it is evident that

the century-scale peak which is centred at around 250 yr is largest for $K_h = 10^3$ m^2/s (the canonical value of the horizontal diffusivity), and that this energy drops off as this parameter increases. This behaviour is consistent with the pattern of decreasing σ_1 in line 2 of Table 4. For large K_h ($= 15 \times 10^3$ m^2/s), however, we note that there is a low-frequency rise in the spectrum, indicating substantial energy at periods longer than about 1 kyr, which is consistent with the spectrum in Fig. 8.

From the front spectrum in Fig. 9b (the case for the canonical diffusivity pair), we observe that the 227-yr peak (which especially stands out in Fig. 7b) is not as large as the approximately 250-yr peak that is so visible in the front spectrum in Fig. 9a (small K_v case). For large K_h, there is a suggestion of some energy at around 500 and 1000 yr; this is due to small-amplitude quasi-periodic fluctuations of this time scale in the corresponding time series (not shown). However, the flow pattern still consists mainly of one large positive cell. When the random forcing is increased to 0.2 Sv, the resulting time series (not shown) contains pronounced 1000–2000 yr oscillations, with F_1 ranging between 0.3 and 0.5 PW. The corresponding streamfunction pattern shows the alternating development and decay of surface-intensified (upper 2 km) negative cell between 15° and 80°S; a positive cell still dominates the flow, however.

For $K_v = 2 \times 10^{-4}$ m^2/s (Fig. 9c), the energy at the century scale is very low for all K_h, except possibly for large K_h (see rear spectrum). The spectrum for this latter case, however, also shows a clear low-frequency rise, indicating approximately millennial scale energy. Finally, we note that for large K_v (Fig. 9d), the case of a very diffusive ocean with a strong thermohaline circulation, the spectra are fairly flat for all K_h and have a relatively low amplitude, indicating that all the steady states for this K_v value are very stable to the random perturbations.

Propagation of salinity anomalies

In the MM-R study of a randomly forced, three-dimensional global ocean circulation model, it was noted that large, quasi-periodic events occurred in a number of time series describing the flow and heat fluxes in the North Atlantic and Southern Ocean. A spectral analysis of the time series revealed a typical period of 320 yr. While this signal stood out most clearly in the time series of the mass transport through Drake Passage, it was also noticeable in the ocean-to-atmosphere heat flux in the North Atlantic (see Fig. 8 in MM-R). MM-R described this oscillation as an "eigenmode" of the thermohaline circulation whose structure spans the entire Atlantic Ocean. To elucidate the nature of this oscillation more clearly, MM-R constructed meridional-plane composites ("snapshots") of the salinity anomaly field every eighth of a cycle (see their Fig. 10). They found that positive and negative salinity anomalies were advected by the thermohaline circulation. The cycle time for the anomalies is about 320 yr.

We present pictures of the salinity anomaly field next which suggest that the approximately 200-yr period oscillations seen in Fig. 6 may correspond to a zonally averaged analogue of the MM-R eigenmode. While a very similar structure is evident, the anomalies here are much smaller than those in MM-R. There are several reasons for this beyond the fact that their model is a 3-D general circulation model. First, the model here uses explicit vertical diffusivity as well as numerical diffusion, whereas MM-R only have small numerical diffusion. Second, it has been shown that the steady-state circulation in MM-R's model is very close to the transition point to a second equilibrium (Maier-Reimer and Mikolajewicz 1989); thus the circulation they studied is likely to exhibit larger deviations of salinity for a given random forcing.

The century-scale eigenmode shows up most clearly in the salinity field because salinity if a free variable at the ocean surface (in contrast to temperature, which is restored to an SST climatology). Thus the surface salinity anomalies evolve independently and are not removed by the freshwater flux anomalies at the surface. Hence salinity is a key variable for the generation and propagation of long-period signals.

Figure 10a shows a 1000-yr salinity climatology for the canonical diffusivity case, and Fig. 10b-f illustrates, in a sequence of snapshots, the time evolution of the salinity anomaly during the cycle AA' (see Fig. 2a). Each anomaly panel represents an average over ten years, centred on the year indicated at the top. From Fig. 10a, we observe that the salinity of the surface waters increases as they move northward from the south polar region because of the evaporation in the low latitudes (see Fig. 1a). The high-salinity surface waters (>35.2 ppt) then sink north of about 50°N and form a deep return flow at depths of 2000 m and greater (a representation of North Atlantic Deep Water (NADW)).

Figure 10b, which shows a snapshot of the salinity anomaly when the transport and meridional heat fluxes are relatively low (see vertical dashed line through point A in Fig. 2a), reveals the presence of a surface-intensified (upper 1000 m) positive (i.e. "salty") anomaly in the Southern Hemisphere and another positive anomaly in the deeper part of the North Atlantic, which represents NADW formed by the previous cycles. Most of the remainder of the upper water column consists of a negative (i.e. "fresh") anomaly, which reduces the meridional density gradient and hence is reponsible for a slowdown of the overturning. The maximum amplitude of this anomaly, which occurs near the surface, is about 0.2 ppt. (This is about one tenth of the strength of the anomaly that MM-R found.) A quarter of a cycle (52 yr) later (Fig. 10c), in response to the increase in transport, the positive surface anomaly in the Southern Hemisphere, has surged northward (nearly as far as the equator), the NADW has moved southward, with a tongue centred at about 36°N. Relatively fresh water now appears in the thermocline in the Southern Hemisphere and down to the bottom in the far north.

Figure 10d shows that after another quarter of a cycle, the Southern Hemisphere salty anomaly has moved
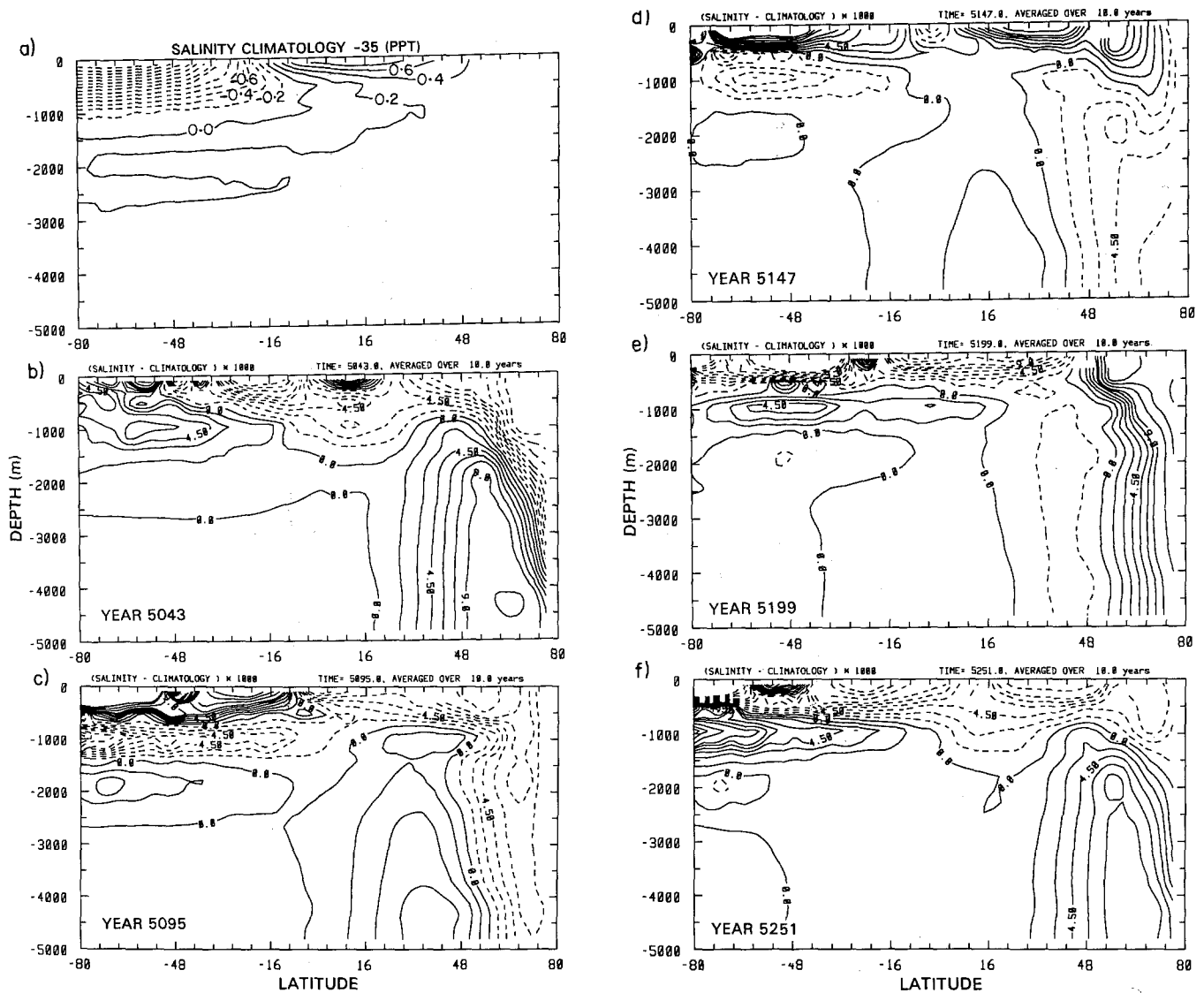
Fig. 10. a Salinity climatology relative to 35 ppt for a thousand-year period beginning at year 5054 (which essentially coincides with point A in Fig. 2a) for the 0.1 Sv randomly forced solution with canonical diffusivities. *Contour interval* is 0.2 ppt; **b** Salinity anomaly relative to the climatology in **a** averaged over a 10-yr period centred at year 5043 (time A in Fig. 2a). *Solid* and *dashed contours* represent positive and negative anomalies respectively. *Contour interval* is 1.5×10^{-3} ppt and contours near the surface that are greater than 18×10^{-3} have been ommitted; **c** As in **b**, but centred at year 5095 approximately a quarter cycle (52 yr) later. **d** As in **b**, but centred at time 5147 yr, approximately a half cycle (104 yr) later. **e** As in **b**, but centred at year 5199, approximately three quarters of a cycle (156 yr) later. **f** As in **b**, but centred at year 5251 (time A' in Fig. 2a), approximately one cycle (208 yr) later

quickly to the northern boundary and begun to sink, pushing the fresh anomaly downward and southward. In the Southern Hemisphere a fresh anomaly slowly moves upward. Another quarter of a cycle later (Fig. 10e) the salty anomaly has sunk to the bottom and the surface waters (south of about 40°N) are characterized by a fresh anomaly. Finally, in Fig. 10f the anomaly pattern is similar to that in Fig. 10b, indicating the the oscillation has essentially completed its cycle.

Figure 10 helps to identify the processes that set up the fluctuations seen in Fig. 2 and demonstrates that they cannot be simply regarded as anomalies that propagate around the entire loop of the thermohaline circulation, which is the case in MM-R. Indeed, if we follow the surface anomalies from south to north, we observe that they are continuously modified. For instance, the large but spatially confined anomaly centred at about 20°S in Fig. 10e has disappeared in the next panel due to mixing with the surrounding strong negative anomalies. Although the anomaly propagates through an evaporative zone (20°S to 20°N, see Fig. 1a), the flow there is in the phase where it is relatively fast. Thus, the positive anomaly does not have time to be replenished and dies (Fig. 10f). Similarly, the fresh pool stretching from 16°S to 40°N in Fig. 10e propagates quickly past the evaporative latitude band unscathed. Once it sinks into the abyss of the high northern latitudes (Fig. 10f), it is no longer affected by surface fluxes but now influences the merid-

ional density gradient (it weakens the latter) and subsequently alters the surface advection field by slowing it down. Thus, upon returning to the early part of the cycle (Fig. 10b, c), where the circulation is reduced, a large positive surface anomaly centred at 20°S propagates slowly through the evaporative zone. It thereby is enhanced and arrives as a strong positive anomaly in the high northern latitudes (Fig. 10d).

From an examination of the whole cycle (Fig. 10b-f), it is apparent that the salinity anomalies get entirely mixed in the deep ocean; thus they are clearly visible in only about half of the 200-year cycle. Thus it would appear that the 200-yr oscillations are generated by the interaction of the variable surface advection field and the $P-E$ distribution through which the salinity anomalies are advected.

Summary and concluding remarks

We have shown that over a wide range of vertical and horizontal diffusivities, the large positive overturning cell that exists under mixed boundary conditions in the Wright-Stocker (WS) thermohaline circulation model is generally stable to a time-dependent white-noise random forcing field superimposed on the freshwater flux boundary condition. For realistic values of K_v (0.5 and $1 \times 10^{-4}\,\mathrm{m^2/s}$) and K_h (10^3 to $10^4\,\mathrm{m^2/s}$), the random forcing exites a basin-wide oscillation which has a period of around 200-300 yr. This mode can be seen clearly in the salinity anomaly field, as a disturbance that is advected near the surface by the meridional overturning cell. It is a zonally averaged analogue of, but is not identical to, the Mikolajewicz-Maier-Reimer 320-yr period eigenmode found in the Atlantic Ocean part of their global ocean model. For larger values of K_v, however, well-defined 200-300 yr oscillations are not excited by the random forcing in the WS model.

For large K_h ($=15 \times 10^3\,\mathrm{m^2/s}$) and small K_v ($=0.5 \times 10^{-4}\,\mathrm{m^2/s}$), a very long-period (deca-millennial) oscillation in the structure of the thermohaline circulation was found. In this weak circulation case, the usual circulation pattern, a large positive cell, changes ("flips") into a large negative cell, passing through a symmetric two-cell circulation in the process. Each circulation state persists for up to 10 kyr, and a transition from one state to the next is relatively rapid (1-2 kyr).

Most of the results presented in this report are for a 0.1 Sv random freshwater forcing in each grid box (corresponding to a $P-E$ flux of about 500 mm/yr). For smaller forcing amplitudes, the century-scale oscillations still exist, but are weaker.

We conclude by mentioning here some extensions that naturally arise out of the present work. First, it would be worthwile using a more realistic meridional profile for the freshwater flux boundary condition. Weaver et al. (1991) showed that the existence and properties of decadal-scale oscillations in a three-dimensional thermohaline circulation model are crucially dependent on the details of this salinity boundary condition. It is conceivable that a similar situation may also apply to century-scale oscillations. Secondly, it is important to determine whether century-scale fluctuations also occur in coupled atmosphere-ocean climate models, such as the one recently developed by Stocker et al. (1992). Clearly, in a coupled model with more realistic feedbacks between the atmosphere and ocean, the nature of internal ocean oscillations could change.

References

Berger A, Melice JL, Hinnov L (1991) A strategy for frequency spectra of Quaternary climate records. Clim Dyn 5:227–240

Boyle EA, Keigwin L (1987) North Atlantic thermohaline circulation during the past 20000 years linked to high-latitude surface temperature. Nature 330:35–40

Broecker WS, Denton GH (1989) The role of ocean-atmosphere reorganizations in glacial cycles. Geochim Cosmochim Acta 53:2465–2501

Broecker WS, Andree M, Wolfli W, Oeschger H, Bonani G, Kennett J, Peteet D (1988) The chronology of the last deglaciation: implications to the cause of the Younger Dryas event. Paleoceanogr 3:1–19

Bryan F (1986) High-latitude salinity effects and interhemispheric thermohaline circulations. Nature 323:301–304

Bryan F (1987) Parameter sensitivity of primitive equation ocean general circulation models. J Phys Oceanogr 17:970–985

Dickson RR, Meinke J, Malmberg SA, Lee AJ (1988) The "Great Salinity Anomaly" in the northern North Atlantic, 1968–82. Prog Oceanogr 20:103–151

Gordon AL (1986) Interocean exchange of thermocline water. J Geophys Res 91:5037–5046

Levitus S (1982) Climatological atlas of the World Ocean. NOAA Prof Paper 13, 177 p

Maier-Reimer E, Mikolajewicz U (1989) Experiments with an OGCM on the cause of the Younger Dryas. In: Ayala-Castañares A, Wooster W, Yáñez-Arancibia A (eds) Oceanography. UNAM Press 87–100

Manabe S, Stouffer RJ (1988) Two stable equilibria of a coupled ocean-atmosphere model. J Climate 1:841–866

Marotzke J, Welander P, Willebrand J (1988) Instability and multiple equilibria in a meridional-plane model of the thermohaline circulation. Tellus 40A:162–172

Mikolajewicz U, Maier-Reimer E (1990) Internal secular variability in an ocean general circulation model. Clim Dyn 4:145–156

Mitchell JM, Dzerdzeevskii B, Flohn H, Hofmeyr WL, Lamb HH, Rao KN, Wallén CC (1966) 'Climatic Change', World Meteorological Organization Technical Note 79, 79 pp

Mysak LA, Manak DK (1989) Arctic sea-ice extent and anomalies, 1953–1984. Atmos-Ocean 27:376–405

Mysak LA, Manak DK, Marsden RF (1990) Sea-ice anomalies observed in the Greenland and Labrador Seas during 1901–1984 and their relation to an interdecadal Arctic climate cycle. Clim Dyn 5:111–133

Pestiaux P, van der Mersh I, Berger A, Duplessy JC (1988) Paleoclimatic variability at frequencies ranging from 1 cycle per 10000 years to 1 cycle per 1000 years: evidence for nonlinear behaviour of the climate system. Clim Change 12:9–37

Priestley MB (1989) Spectral analysis and time series. Academic Press, San Diego

Roemmich D, Wunsch C (1985) Two transatlantic sections: meridional circulation and heat flux in the subtropical North Atlantic Ocean. Deep Sea Res 32:619–664

Rooth C (1982) Hydrology and ocean circulation. Prog Oceanogr 11:131–149

Saltzman B (1990) Three basic problems of paleoclimatic modeling: a personal perspective and review. Clim Dyn 5:67–78

Stocker TF, Mysak LA (1992) Climatic fluctuations on the century time scale: a review of high-resolution proxy data and possible mechanisms. Clim Change 20:227–250

Stocker·TF, Wright DG (1991a) A zonally averaged ocean model for the thermohaline circulation. Part II: Interocean circulation in the Pacific-Atlantic basin system. J Phys Oceanogr 21:1725–1739

Stocker TF, Wright DG (1991b) Rapid transitions of the ocean's deep circulation induced by changes in surface water fluxes. Nature 251:729–732

Stocker TF, Wright DG, Mysak LA (1992) A zonally averaged, coupled ocean-atmosphere model for paleoclimatic studies. J Climate 5 (in press)

Stommel H (1961) Thermohaline convection with two stable regimes of flow. Tellus 13:224–230

Weaver AJ, Sarachik ES (1991a) The role of mixed boundary conditions in numerical models of the ocean's climate. J Phys Oceanogr 21:1470–1493

Weaver AJ, Sarachik ES (1991b) Evidence for decadal variability in an ocean general circulation model: an advective mechanism. Atmos Ocean 29:197–231

Weaver AJ, Sarachik ES, Marotzke J (1991) Freshwater flux forcing of decadal and interdecadal oceanic variability. Nature 353:836–838

Wright DG, Stocker TF (1991) A zonally averaged ocean model for the thermohaline circulation. Part I: Model development and flow dynamics. J Phys Oceanogr 21:1713–1724

Wright DG, Stocker TF (1992) Sensitivities of a zonally averaged global ocean circulation model. J Geophys Res 91 (in press)

Yiou P, Genthon C, Ghil M, Jouzel J, Le Treut H, Barnola JM, Lorius C, Korotkevitch YN (1991) High-frequency paleovariability in climate and CO_2 levels from Vostock ice core records. J Geophys Res 96:20365–20378